Acta Montanistica Slovaca
ISSN 1335-1788
actamont.tuke.sk

Bivariate Analysis of Discomfort Index and Remote Sensing Ecological Vulnerability Index Using Statistical Patterns and Color Matrix Relationships

***Vladimir ONDREJICKA*[1]*, *Firouz AGHAZADEH*[2], *Akbar RAHIMI*[3] *and* *Maros FINKA*[4]**

Authors' affiliations and addresses:
[1] SPECTRA Centre of Excellence, Department of Environmental Management and Spatial Planning, Faculty of Management, Comenius University in Bratislava, Odborárov 10, Bratislava.
e-mail: ***vladimir.ondrejicka@fm.uniba.sk***

[2] SPECTRA Centre of Excellence, Department of Environmental Management and Spatial Planning, Faculty of Management, Comenius University in Bratislava, Odborárov 10, Bratislava.
e-mail: ***Aghazadeh1@uniba.sk***

[3] Department of Urban and Regional Planning, Faculty of Planning and Environmental Sciences, University of Tabriz, Tabriz, Iran
e-mail: ***akbar.rahimi@gmail.com***

[4] SPECTRA Centre of Excellence, Department of Environmental Management and Spatial Planning, Faculty of Management, Comenius University in Bratislava, Odborárov 10, Bratislava.
e-mail: ***maros.finka@uniba.sk***

***Correspondence:**
SPECTRA Centre of Excellence, Department of Environmental Management and Spatial Planning, Faculty of Management, Comenius University in Bratislava, Odborárov 10, Bratislava.
e-mail: ***vladimir.ondrejicka@fm.uniba.sk***

Funding information:
This research was supported by the Recovery and Resilience Plan of SR, co-financed by the European Union through NextGeneration EU under contract nr. 09I02-03-V01-00011 – project Smart Transformation and Innovation Consortium Slovakia (STICS).

How to cite this article:
Ondrejicka, V., Aghazadeh, F., Rahimi, A. and Finka, M. (2025), Bivariate Analysis of Discomfort Index and Remote Sensing Ecological Vulnerability Index Using Statistical Patterns and Color Matrix Relationships. *Acta Montanistica Slovaca*, Volume 30 (4), 1060-1078

DOI:
https://doi.org/10.46544/AMS.v30i4.16

Abstract
The relationship between ecological vulnerability (EV) and the Discomfort Index (DI), which manifests the coupled dynamics of ecological fragility and climatic stress, remains inadequately quantified in a spatially explicit manner. In this study, multi-temporal Landsat 5 and 8 imagery and ERA5-Land reanalysis data were integrated to construct a remote-sensing ecological vulnerability index (RSEVI) through Principal Component Analysis of wetness, heat, greenness, dryness, and land degradation indicators. In parallel, DI was derived from land surface temperature and relative humidity. Spatial dependencies between the two indices were assessed using the bivariate L statistic, complemented by bivariate color mapping, to visualize synchronous clusters. The results reveal pronounced shifts between 2000 and 2025: the mean DI increased from 23.31 °C to 26.79 °C, while areas under "medical emergency" conditions expanded from 0.1% to 8.6%. Simultaneously, the share of strongly and extremely vulnerable areas will increase from 5.5% in 2000 to 18.9% in 2025. Spatial association analysis reveals a significant increase in high-high clusters (high vulnerability–high discomfort) from 48% to 74%, primarily concentrated in the southern and eastern sectors. Conversely, low-low clusters increased from 23% to 34%, consolidating resilient cores in the north. Discordant clusters exhibited divergent trajectories: low-high associations expanded from 28% to 48%, while high-low clusters remained relatively stable (~39%). These patterns underscore the dual emergence of critical hotspots and resilient strongholds while intensifying spatial heterogeneity. By developing a spatially robust framework, this study avoids spatial fallacies and provides tools to identify hotspots and resilient areas, offering a replicable method for environmental risk assessment and adaptive planning under climate change.

Keywords
Remote Sensing Ecological Vulnerability Index, Discomfort Index, Bivariate Spatial Association, Bivariate Spatial Relationship Color Mapping, Bratislava City.

Introduction

Global climate change and anthropogenic pressures are increasingly undermining the ecological equilibrium of Earth, pushing ecosystems toward heightened sensitivity, instability, and functional degradation (Pimm et al., 2014; Dinerstein et al., 2019; Lin et al., 2023). The prominent manifestations of these processes include global warming, desertification, soil erosion, biodiversity collapse, shifts in precipitation regimes, and freshwater availability (Santini et al., 2019; Huang et al., 2023; Yuan et al., 2024). The significance of these transformations is not confined to natural systems; human dimensions are also directly affected by the thermal exposure and bioclimatic comfort of populations (Gao & Zhang, 2018; Tian et al., 2021; Wang et al., 2021). Hence, establishing a systematic link between "ecological quality" and "bioclimatic discomfort" is a pivotal prerequisite for risk management, climate adaptation, and territorial planning (Alonso & Renard, 2020).

Over the past two decades, EV assessments have been extensively developed across multiple scales, with diverse models and indices being proposed (Ameur et al., 2019). Representative examples include the DPSIRM and SD frameworks in the Yenma Basin (Zhang et al., 2017), spatial principal component analysis in East Asia (Kang et al., 2018), dynamic weighting in the karst landscapes of Southwest China (Guo et al., 2020), and complex network models for evaluating urban ecological responses in Wuhan (Wang et al., 2020). Several studies have developed automated and data-driven frameworks for EV evaluation (Xia et al., 2021; Tang et al., 2021; Hu et al., 2021). In particular, the Remote Sensing Ecological Index (RSEI) and its extension into the RSEVI, integrating greenness, dryness, wetness, and temperature, have emerged as standard tools for ecological quality monitoring (Yang & Song, 2021; Zhang et al., 2021; GUO et al., 2024).

However, fundamental challenges persist in this regard. In arid regions, plateaus, and data-scarce territories, the paucity of field and statistical observations necessitates the advancement of large-scale remote-sensing indices (Ma et al., 2020). Integrating remotely sensed imagery with socioeconomic datasets (e.g., VIIRS and DMSP-OLS) has been demonstrated as an effective strategy to overcome these data limitations (Guo & Wen, 2020; Guo et al., 2020). Examples include the China–Pakistan Economic Corridor (CPEC), which is experiencing pronounced climate change, desertification, and anthropogenic stresses (Li et al., 2020); the Yellow River Basin, central to China's national conservation and high-quality development agenda (Bai et al., 2023; Wang et al., 2023; Huang et al., 2023); and Mongolia, recognized as a global hotspot of desertification (Han et al., 2025). These investigations highlight the necessity for long-term monitoring to identify trends and dominant drivers (You et al., 2023; Yuan et al., 2024).

From the human dimension, DI, formulated based on air temperature and relative humidity (Thom, 1959), has served as a canonical benchmark in climate–health research and environmental design (ANSI/ASHRAE 55, 1992; EN 15251, 2007). This index has been employed across diverse settings, ranging from the Mediterranean (Alonso & Renard, 2020) to tropical environments (Da Silva et al., 2010) and megacities characterized by intense urban heat island effects (Xu et al., 2017). Empirical evidence has demonstrated that urban green cover, through evapotranspiration, effectively mitigates DI (Da Silva et al., 2010; Aghazadeh et al., 2025). More recently, studies in Southern Europe have underscored that escalating DI trajectories, in conjunction with demographic aging and intensifying heat waves, exacerbate public health risks (Monforte & Ragusa, 2022; Ebi et al., 2006; Renard et al., 2020).

Despite the relative maturity of the EV and DI research domains, their spatial–statistical integration remains insufficiently addressed in the literature. Most prior studies have relied on non-spatial correlations, thereby risking spatial fallacies (Anselin 1995). Conversely, the bivariate L statistic (Lee, 2001; Lucas et al., 2025; Illanas et al., 2025), which synthesizes the Pearson correlation with spatial dependence akin to Moran's I, provides a robust framework for spatially explicit correlation analysis (Tao & Thill, 2025). Moreover, the "bivariate color relationship mapping" approach, employing four-quadrant segmentation (high–high, high–low, low–high, low–low), offers a powerful visualization tool for detecting synchronous clusters such as "high vulnerability - high discomfort" and "low vulnerability - low discomfort" (Jankowski et al., 2024; Pak et al., 2024; Alyaqout et al., 2025; Schlögl et al., 2025).

Accordingly, the present study aims to (i) develop the RSEVI by incorporating wetness, thermal, greenness, dryness, and land degradation components for the period 2000–2025 using a PCA-based approach (Guo & Wen, 2020); (ii) compute the DI based on temperature and humidity data (Thom, 1959; ASHRAE 55, 1992); and (iii) analyze their spatially explicit interrelationships via the bivariate Lee index and Spatial P-values. In addition, by applying a spatial bivariate color-mapping framework, spatial clusters were visualized to illustrate synchronous vulnerability–discomfort patterns. The novelty of this study lies in three dimensions: (i) establishing a quantitative, spatially explicit nexus between EV and DI; (ii) employing spatial–statistical methodologies to circumvent spatial fallacies; and (iii) providing policy-oriented visualization tools to translate analytical outputs into actionable recommendations for spatial management and climate adaptation. This research bridges existing gaps and offers a comprehensive, replicable, and generalizable framework for the integrated assessment of ecological and human dimensions.

Material and Methods

Study area

This study focuses on the city of Bratislava, the capital of Slovakia, located in the southwestern part of the country near the borders of Austria and Hungary (48.14944° N, 17.07333° E) (Fig.1). Bratislava lies within a temperate continental climate zone with a mean annual temperature of approximately 10 °C and an average annual precipitation of 738 mm. The municipal territory covers an area of 367.66 km² and is administratively divided into five districts (Šalkovič and Pauditšová, 2023). With a population of 475,503 inhabitants as of 2021, Bratislava represents both the largest and the most populous city in Slovakia (Statistical Office of the Slovak Republic, 2022). The city's natural setting is strongly shaped by the Danube River, which flows directly through its urban core, and the Malé Karpaty (Small Carpathians) mountain range, which extends into its northern part. The Morava River delineates its western boundary. The elevation ranges from 126 m above sea level at the lowest point to 514 m at Devínska Kobyla, the city's highest peak. To the south, the foothills of the Small Carpathians descend into the Danubian Lowland, whereas the northern sector opens into the Záhorská Lowland (Belčáková et al., 2022). Bratislava is a representative Central European urban area, characterized by a mosaic of vegetation types, including forests, parks, gardens, cemeteries, lawns, and ruderal habitats. Although urban greenery accounts for nearly 30% of a city's territory, its distribution is markedly uneven (Bobáunková et al. 2024). The study area was selected based on the spatial and ecological diversity of vegetation within both the urban and peri-urban zones. Of particular interest are ruderal plant communities, which form the principal subject of this study (Belčáková et al., 2022).

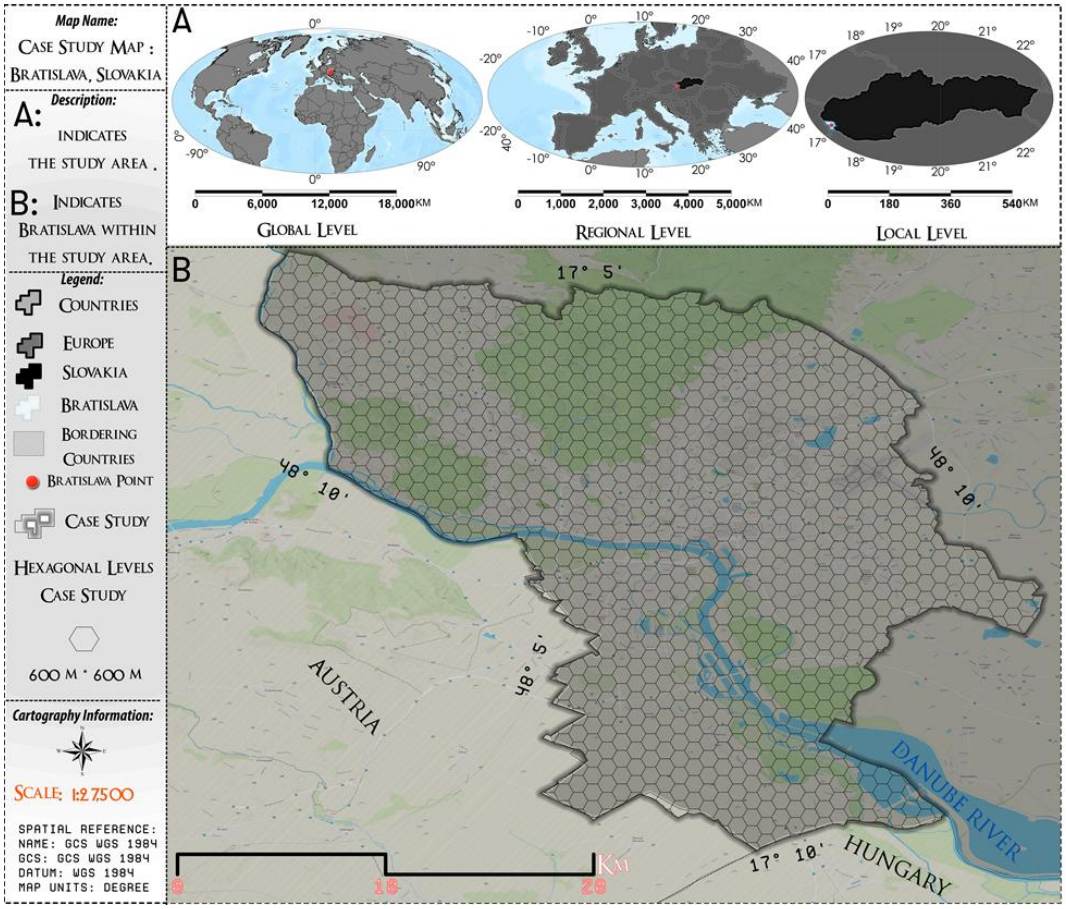

Fig 1. The geographical location of Bratislava, the capital of Slovakia

Data

In this study, an integrative framework comprising satellite observations and reanalysis products was employed to analyze the ecological vulnerability and discomfort indices. The primary datasets consisted of Landsat 5 and Landsat 8 imagery, alongside ERA5-Land reanalysis products provided by the European Center for Medium-Range Weather Forecasts (ECMWF). Optical and thermal Landsat data were utilized to derive ecological and thermal indicators with a spatial resolution of 30 m for the optical bands and 120/100 m for the thermal bands. In

this study, however, resampled thermal data from Level-2 products at 30 m resolution were applied. These data, with a temporal resolution of 16 days, cover the years 2000, 2015, and 2025, with a particular focus on the summer months (July–September). Only scenes with less than 10% cloud cover were selected, and all images were subjected to radiometric calibration to ensure data accuracy. During the processing phase, surface reflectance products were employed to compute urban indices, including the Normalized Difference Built-up Index (NDBI) and Bare Soil Index (BSI). In parallel, Land Surface Temperature (LST) maps were generated from the thermal bands. To assess the vegetation conditions, the Normalized Difference Vegetation Index (NDVI) and Leaf Area Index (LAI) were derived. The Soil Water Content Index (SWCI) was calculated to examine surface dryness, whereas land degradation was assessed using surface albedo, Salinity Index (SI), and Topsoil Grain Size Index (TGSI). Complementarily, ERA5-Land datasets with a spatial resolution of 9 km and hourly temporal resolution were used to extract and compute relative humidity (RH). The entire process of data handling, computation, and indicator extraction was conducted using the cloud-based Google Earth Engine[1] platform. Ultimately, the integration of satellite observations and reanalysis data enables a comprehensive analysis of thermal fluctuations and ecological vulnerability. The temporal and spatial details of the datasets used in this study are presented in Table 1.

Table 1. Specifications of the datasets employed in this research

Index		Satellite and dataset	Collection	Spatial Resolution	Temporal Resolution	Research Period	
Moisture (SWCI)		Landsat 5 & 8	Landsat/LT05 & LC08/ C2_L2	Landsat 5 & 8 optical= 30 Thermal= 120 & 100m Resampled =30 m	16 Day	2000-2015-2025	July- September
Heat (LST)							
Greenness (GI)	NDVI						
	LAI						
Dryness (NDSI)	NDBI						
	BSI						
Land degradation (LDI)	Albedo						
	SI						
	TGSI						
ERA5-Land	RH1	ECMWF	ECMWF/ERA5_LAND/HOURLY	9km	Hourly		

The conceptual model developed in this study integrates remote sensing data, ecological indices, and advanced spatial–statistical analyses to provide a comprehensive framework for environmental vulnerability assessment. In the first stage, multi-temporal Landsat 5 and 8 satellite imagery was acquired and pre-processed within the GEE platform. From these datasets, a suite of key ecological indicators was derived, including LST, SWCI, GI, NDSI, and LDI. These indices collectively serve as essential descriptors of the landscape ecological conditions. Subsequently, data processing and dimensionality reduction were performed using Python in Google Colab. Principal Component Analysis (PCA) was applied to mitigate multicollinearity and integrate the selected indices into a composite metric, thereby deriving the RSEVI. In parallel, the DI, which reflects bioclimatic stress and its potential implications for human and ecological well-being, was calculated. In the final stage, both RSEVI and DI were integrated into the ArcGIS Pro platform to conduct advanced spatial association analyses. Specifically, Bivariate Local Spatial Association (Lee's L-index) and its statistical significance (p-value LEE) were employed to capture the spatial dependence and clustering patterns of the two indices. To further enhance interpretability, Spatial Bivariate Relationship Color Mapping was applied, enabling visualization of positive and negative spatial associations in the form of a bivariate color matrix. This approach provides a robust means of simultaneously examining spatial variations in both indices, thereby offering nuanced insights into the coupled dynamics of ecological vulnerability and bioclimatic discomfort. Overall, the proposed conceptual model established a rigorous integrative framework for assessing the bidirectional relationships between ecological vulnerability and environmental discomfort. By combining remote sensing observations, advanced statistical methods, geospatial analysis, and color-matrix visualization, this study contributes to a scientifically robust methodology for monitoring environmental dynamics and assessing ecological risk across regional scales (Fig 2).

1 - Relative Humidity

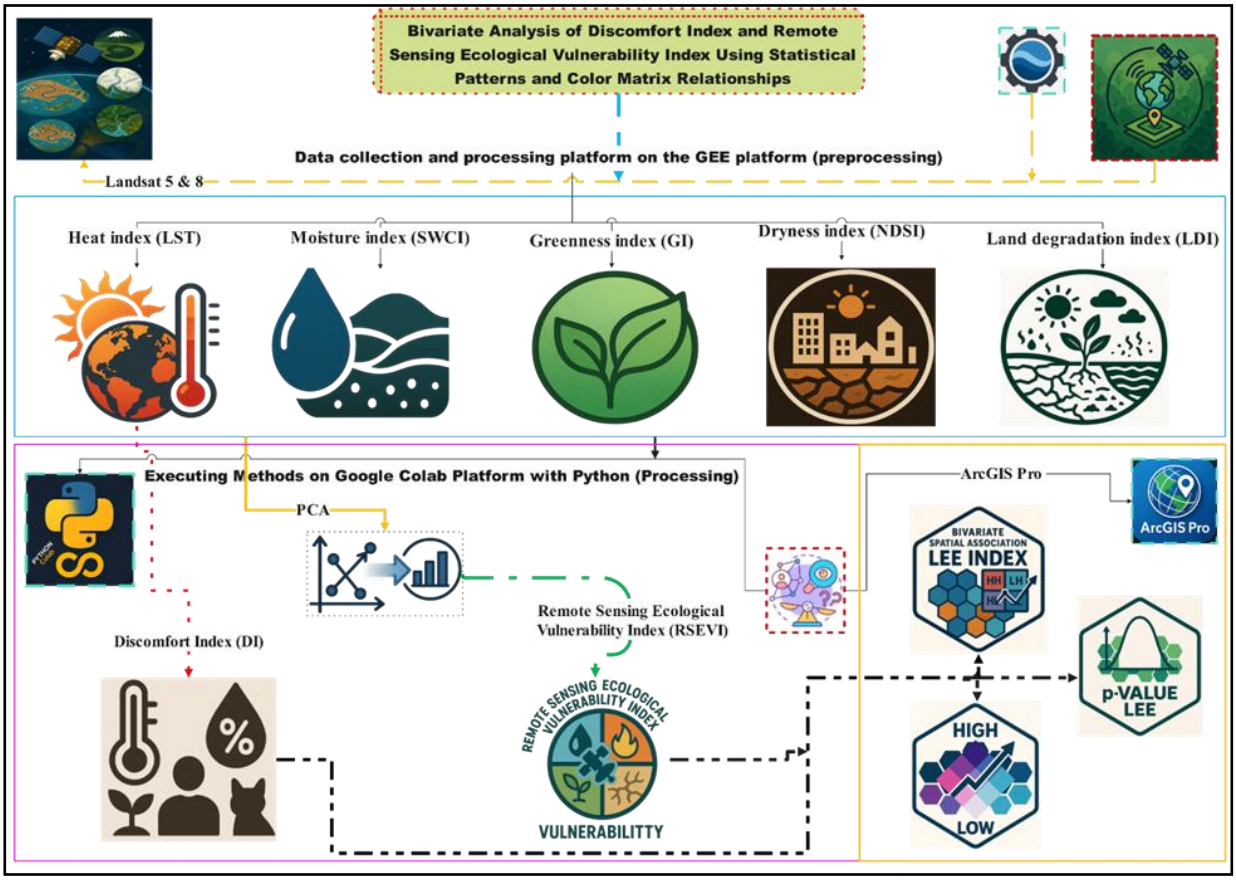

Fig 2. Conceptual Model of Remote Sensing–Driven Ecological Vulnerability and Bioclimatic Discomfort: An Integrated Approach Using Multivariate Indices and Spatial Bivariate Color Mapping

Methodology

Quantification of the remote sensing ecological Vulnerability Index (RSEVI)

In this study, remote sensing observations from Landsat 5 (TM) and Landsat 8 (OLI/TIRS) were used to derive a suite of ecological indicators. Owing to their extensive temporal coverage, broad spatial extent, and robust spectral resolution, these datasets provide a reliable foundation for the regional-scale monitoring of ecosystem dynamics. Five core dimensions were assessed: surface moisture, thermal conditions, vegetation greenness, soil dryness, land degradation, and anthropogenic pressures.

Moisture index

Soil and surface moisture represent fundamental controls on terrestrial ecosystems, directly influencing the energy balance, water cycling, and vegetation dynamics (Eq. 1)

$$SWCI_{landsat\ 5} = \frac{B_5 - B_7}{B_5 + B_7} \quad , \quad SWCI_{landsat\ 8} = \frac{B_6 - B_7}{B_6 + B_7} \tag{1}$$

Greenness index

Vegetation is a fundamental component of terrestrial ecosystems, exerting a decisive influence on ecosystem structure and functioning and contributing to the stability of regional ecological systems. In this study, the Normalized Difference Vegetation Index (NDVI) and Leaf Area Index (LAI) were employed to construct a composite greenness index, which provides a more accurate representation of vegetation vigor and canopy density (Eq. 2). These indicators are widely recognized for their effectiveness in characterizing vegetation dynamics and ecological resilience (Wang et al., 2010; Ma et al., 2020).

$$GI = \frac{NDVI + LAI}{2} \tag{2}$$

Dryness index

In arid and semi-arid regions, soil desiccation constitutes a major ecological constraint. To characterize this dimension, the Normalized Difference Barren Index (NDBI) and Bare Soil Index (BSI) were integrated to construct the Normalized Dryness Soil Index (NDSI) (Eq 3-5). This indicator provides a spatially explicit measure of water scarcity and soil aridity, thereby enhancing the assessment of drought-induced ecological vulnerability (Lu et al. 2022).

$$NDBI_{landsat\ 5} = \frac{B_5 - B_4}{B_5 + B_4} \quad , \quad NDBI_{landsat\ 8} = \frac{B_6 - B_5}{B_6 + B_5} \tag{3}$$

$$BSI_{landsat\ 5} = \frac{(B_5 + B_3) - (B_4 + B_1)}{(B_5 + B_3) + (B_4 + B_1)} , BSI_{landsat\ 8} = \frac{(B_6 + B_4) - (B_5 + B_2)}{(B_6 + B_4) + (B_5 + B_2)} \tag{4}$$

$$NDSI = \frac{NDBI + BSI}{2} \tag{5}$$

Land degradation index

Land degradation processes, including desertification, salinization, and soil erosion, are significant threats to ecological integrity. To quantify these processes, a composite Land Degradation Index (LDI) was developed by combining the surface albedo, soil salinity, and topsoil grain size parameters (Eqs. 6-9). This index provides a holistic representation of degradation intensity and its ecological consequences (Guo et al., 2024; Bahta et al., 2019).

$$Albedo = 0.001 * M \tag{6}$$

$$SI_{landsat\ 5} = \sqrt{B_3 * B_1} \quad , \quad SI_{landsat\ 5} = \sqrt{B_4 * B_2} \tag{7}$$

$$TGSI_{landsat\ 5} = \frac{B_3 - B_1}{B_3 + B_1 + B_2} \quad , \quad TGSI_{landsat\ 8} = \frac{B_4 - B_2}{B_4 + B_2 + B_3} \tag{8}$$

$$LDI = \frac{Albedo + SI + TGSI}{3} \tag{9}$$

Heat index or Land Surface Temperature (LST)

The LST is a critical determinant of ecological functioning, shaping vegetation growth, distribution patterns, and evapotranspiration rates. It also serves as a sensitive indicator of drought severity and thermal stress, thereby offering valuable insights into the interactions between climate variability and ecosystem responses (Lu et al. 2022). LST, derived from resampled Level-2 Landsat products with a spatial resolution of 30 m, provides a reliable foundation for analyzing the thermal regulation capacity of urban green spaces, particularly given their often limited spatial coverage. In this study, LST values for peak summer conditions, defined as the average across July, August, and September, were calculated using data from the Landsat 5 and Landsat 8 missions (Aghazadeh et al., 2025). The pre-processing procedure commenced with the conversion of thermal band Digital Number (DN) values into physically meaningful surface temperature indicators (Rees et al., 2024). All the images were obtained from the United States Geological Survey (USGS) archive. Following the methodological framework outlined in the Landsat Product Guide (Worsa-Kozak et al., 2024), the LST derivation was implemented using the Google Earth Engine cloud platform (Aghazadeh et al., 2025). Initially, radiometric scaling factors were applied to convert DN values into Kelvin, which were subsequently transformed into Celsius values. The mathematical formulation applied for this conversion is given by Eq. (10).

$$LST = (DN * 0.00341802 + 149.0) - 273.15 \tag{10}$$

In this context, LST refers to the land surface temperature expressed in degrees Celsius, and DN indicates the digital number assigned to each raster pixel. The expression 0.00341802 + 149.0 functions as the calibration factor, and the constant 273.15 is applied to convert temperature values from Kelvin to Celsius.

Principal Component Analysis (PCA)

PCA is a robust statistical technique that is employed for dimensionality reduction and feature extraction in high-dimensional datasets. This method transforms the original variables into a new set of uncorrelated components, defined as linear combinations, which capture the maximum variance within the data while preserving the essential information. These components, which are derived through the computation of eigenvalues and eigenvectors of the covariance matrix, ensure orthogonally and effectively represent the primary structure of the dataset with minimal information loss (Chen et al., 2025; Xu et al., 2025).

Derivation of a Remote Sensing–Driven Ecological Vulnerability Index

To integrate these multiple dimensions, PCA was applied to construct a composite RSEVI. This multidimensional index (Eq. 11) not only enables a comprehensive evaluation of ecosystem fragility but also captures spatiotemporal patterns of ecological vulnerability driven by climatic stressors and anthropogenic disturbances. As such, the RSEVI provides a robust framework for quantifying ecosystem resilience under complex environmental changes (Han et al., 2025; Guo et al., 2024).

$$RSEVI = a_1 * P_1 + a_2 * P_2 + \cdots + a_x * P_x \quad (11)$$

Discomfort Index (DI)

DI has emerged as a widely applied indicator for quantifying human thermal stress across diverse climatic regimes, particularly during periods of elevated summer heat (Ekra et al., 2024). This index conceptualizes thermal comfort primarily as a function of two meteorological determinants: ambient air temperature (Ta) and relative humidity (RH) (Thom, 1959). Subsequent refinements by Epstein and Moran established the *DI* as a standardized and universally applicable metric for evaluating thermal perception (Zeng et al., 2024). The mathematical formulation is expressed in Eq. (12):

$$DI = Ta - 0.55\,(1 - 0.01RH)\,(Ta - 14.5) \quad (12)$$

Where *Ta* denotes the air temperature and RH represents the relative humidity.

In the present study, LST was employed as a surrogate variable for *Ta* (Imran et al., 2021). The relative humidity values were derived from the ERA5-Land reanalysis dataset. Given that ERA5-Land does not provide RH directly, estimations were generated using the dew point temperature and near-surface air temperature using the empirical relation in Eq. (13) (Bonshoms et al., 2022):

$$RH_{2m} = 100 - 5 * (T_{2m} - Td_{2m}) \quad (13)$$

Furthermore, the DI values were categorized into six discrete thermal comfort classes according to the classification proposed by Patle and Ghuge (2024), as summarized in Table 2.

Table 2. Discomfort ranges and conditions

Class number	DI (°C)	Discomfort conditions
1	DI <21	No discomfort
2	21≤ DI <24	Less than half of the population feels discomfort
3	24≤ DI <27	More than half of the population feels discomfort
4	27≤ DI <29	Most of the population suffers discomfort
5	29≤ DI <32	Everyone feels severe stress
6	≥32	State of medical emergency

Local Bivariate Spatial Association (Lee's L)

Lee (2001) maintained that a rigorous index for bivariate spatial autocorrelation should be capable of simultaneously capturing the co-location patterns of variables by integrating both inter-variable covariance and the spatial configuration of observations. To operationalize this premise, he proposed a bivariate spatial autocorrelation (BSA) index that unifies Pearson's correlation coefficient as a measure of direct pairwise association with Moran's I, the canonical metric of spatial dependence. The localized expression of this statistic, denoted as Lee's L in Equation (15), adopts the same notation as in Eq. (14), with both variables normalized to zero mean and unit variance. Parameter n indicates the total number of observations in the dataset. This formulation alleviates the asymmetry inherent in the BI_i statistic; however, its multiplicative structure continues to overemphasize the contribution of extreme values. Analogous to BIi, Lee's L partitions spatial associations into

four canonical cluster types: high–high (HH), low–low (LL), low–high (LH), and high–low (HL) (Lee, 2017). Nonetheless, the present study challenges several of the foundational assumptions in Lee's (2001) framework and advances two alternative propositions: (1) a valid bivariate spatial index does not necessarily require an explicit decomposition between covariance and spatial clustering effects, and (2) additional local manifestations of BSA, beyond those strictly driven by extreme values, can reasonably be anticipated.

$$BI_i = cx_i \sum_j w_{ij} y_j \tag{14}$$

Eq. (15) defines the bivariate local Moran's I (BI_i), which quantifies the localized BSA for a given region, *i*. Specifically, x_i denotes the value of variable *x* in region *i*, and y_j represents the value of variable *y* in region *j*. Spatial weight wij reflects the adjacency or spatial interaction between regions *i* and *j*, whereas *c* functions as a scaling constant.

$$L_i = \frac{n(\sum_j w_{ij} x_j)(\sum_j w_{ij} y_j)}{\sqrt{\sum_i x_i{}^2}\ \sqrt{\sum_i y_i{}^2}} \tag{15}$$

By definition, BI_i is the product of x_i and the spatial lag of *y*, with both variables standardized to have zero mean and unit variance (Anselin, 2019).

Bivariate Spatial Relationship

The proposed analytical framework for bivariate spatial relationships was designed to systematically characterize and interpret the interdependencies between paired variables across geographic spaces. To achieve this, the framework applies a calibrated spectrum of color gradients that classifies variables into distinct visual categories, thereby generating spatial representations that convey the magnitude and direction of relationships with clarity. In situations where variable overlaps reduce interpretability, normalization procedures are incorporated to enhance visualization precision. The framework encompasses four principal configurations: transparent overlays, sequential–sequential schemes, diverging–diverging schemes, and qualitative–sequential schemes. In the present study, a sequential–sequential configuration was employed (Brewer, 2016).

Sequential–Sequential Configuration

The sequential configuration is tailored to analyze spatial linkages among two or more quantitative attributes associated with defined geographic units. This design is particularly suited to vector-based datasets containing attribute fields that enable robust statistical assessment. A distinctive advantage of this configuration is its ability to represent continuous spatial transitions, allowing researchers to detect the underlying gradients and identify clustering phenomena. For instance, urban studies can reveal relationships between concentrations of vacant properties and local crime rates, providing empirical insights for policymakers evaluating whether property neglect contributes to heightened crime levels. Beyond urban contexts, the configuration has notable applications in economic geography—for examining spatial correlations between household income and property values—and in agricultural research, where it can uncover linkages between soil quality and crop yield. More broadly, this approach facilitates the detailed detection of spatial trends in quantitative datasets, strengthens predictive modeling grounded in historical trajectories, and supports the identification of high-risk areas requiring targeted policy interventions (Brewer, 2016).

Results

Dynamics of Environmental Indicators Influencing Ecological Vulnerability (2000–2025)

The temporal dynamics of the RSEVI components from 2000 to 2025 reveal a complex interplay between reinforcing and counteracting processes. The steady increase in GI (from 1.08 to 1.23) reflects a gradual improvement in green infrastructure, which theoretically enhances ecological resilience. However, this positive trend was not sufficient to counterbalance the pronounced increase in LST, which increased by more than 5°C over the 25-year period. The increase in surface temperature indicates a strong urban heat island effect, suggesting that the benefits of expanding green spaces have been partially offset by intensified land-use changes and the proliferation of impervious surfaces. Meanwhile, LDI remained relatively stable, showing no substantial fluctuations at the regional scale. Nevertheless, the decline in NDSI (from -0.14 to -0.18) points toward a gradual deterioration of soil conditions, likely driven by subtle but persistent land degradation processes. This trend suggests increasing ecological vulnerability in terms of soil quality, which is a critical component of ecosystem functioning. Interestingly, SWCI displayed a slight upward trend (from 0.267 to 0.281), implying modest

improvements in soil water availability. Although this change is relatively minor, it may serve as a mitigating factor, buffering ecosystems against the adverse effects of increasing land surface temperature and soil degradation. Overall, the trajectory of these indices underscores a paradox: while green infrastructure and soil water content show positive tendencies, the concurrent intensification of heat stress and soil degradation highlights persistent and possibly escalating ecological vulnerability. These results emphasize that strengthening the RSEVI requires integrated management strategies that simultaneously address green infrastructure expansion, urban heat mitigation, and soil conservation (Tab 3).

Table 3. Temporal Variation in the Average Values of Key Environmental Indicators

Indicators / Year	2000	2015	2025
GI	1.08	1.16	1.23
LDI	0.084	0.081	0.082
LST	25.50	27.26	30.50
NDSI	-0.14	-0.16	-0.18
SWCI	0.267	0.270	0.281

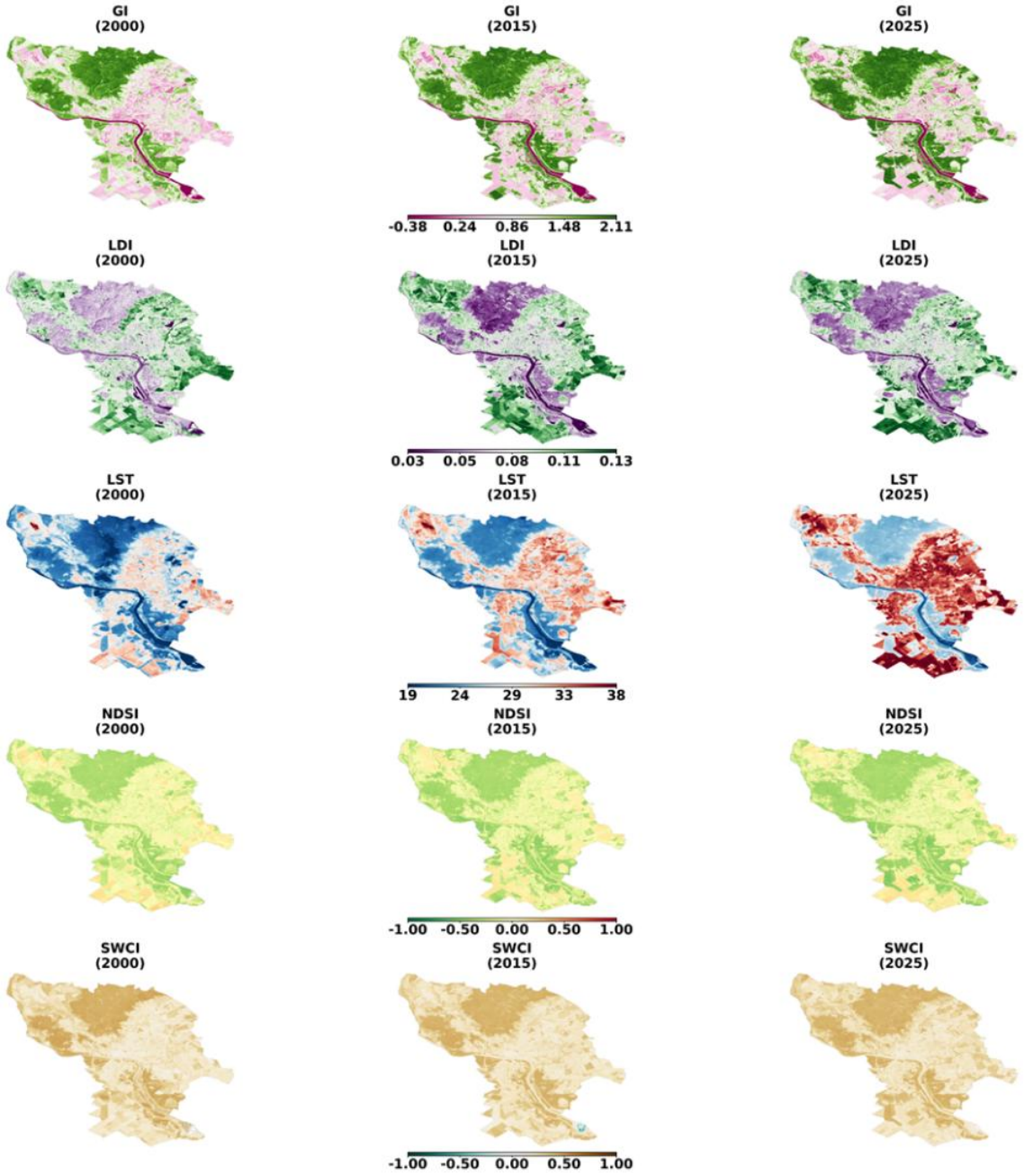

Fig 3. Spatio-Temporal Dynamics of Environmental Indicators across the Study Area

The spatial maps of the indices collectively revealed a coherent trajectory of change over the study period. In the GI maps, green infrastructure gradually expanded, with denser and more continuous patches becoming evident, particularly across the northern and central zones in the later years. In contrast, the LDI maps displayed relatively minor and scattered variations, with only subtle intensifications in the central parts over time. The LST sequence illustrates a pronounced transformation, as cooler areas in the initial map were progressively replaced by warmer zones, culminating in widespread red patches in the final stage, clearly indicating the dominance of higher surface temperatures. The NDSI maps appeared more uniform, yet a subtle but consistent shift toward more negative values was visible, most notably in the southern areas, reflecting an increasing prevalence of lower index values. Finally, the SWCI maps remained comparatively stable, although slight improvements were noticeable at the periphery in the later period. Taken together, the maps convey a continuous and integrated picture of spatiotemporal dynamics, capturing a gradual yet profound transformation of the ecological landscape across the study horizon.

Spatiotemporal Dynamics of Ecological Vulnerability Based on the RSEVI Index (2000–2025)

The spatiotemporal evolution of the RSEVI index between 2000 and 2025 reveals a marked transition from relatively stable conditions toward an increasingly fragile ecological system. Statistically, the minimum values fluctuate substantially, shifting from –5.96 in 2000 to –2.71 in 2015 before declining again to –4.26 in 2025. This pattern indicates that highly fragile zones have not only persisted but, in some cases, intensified over time. In contrast, the maximum values exhibited a steady upward trend, rising from 3.93 in 2000 to 5.00 in 2025, which underscores the emergence and consolidation of extreme vulnerability hotspots. The mean values also show a systematic drift from –0.10 in 2000 to 0.15 in 2025, signifying an overall shift toward greater vulnerability. Meanwhile, the progressive increase in standard deviation, from 1.31 to 1.50, highlights growing spatial heterogeneity and a widening disparity between low- and high-vulnerability areas. Spatial distribution maps provide compelling visual evidence of these statistical trends. In 2000, the landscape was predominantly dominated by zones of negligible vulnerability (dark blue), with scattered patches of light or medium vulnerability. By 2015,

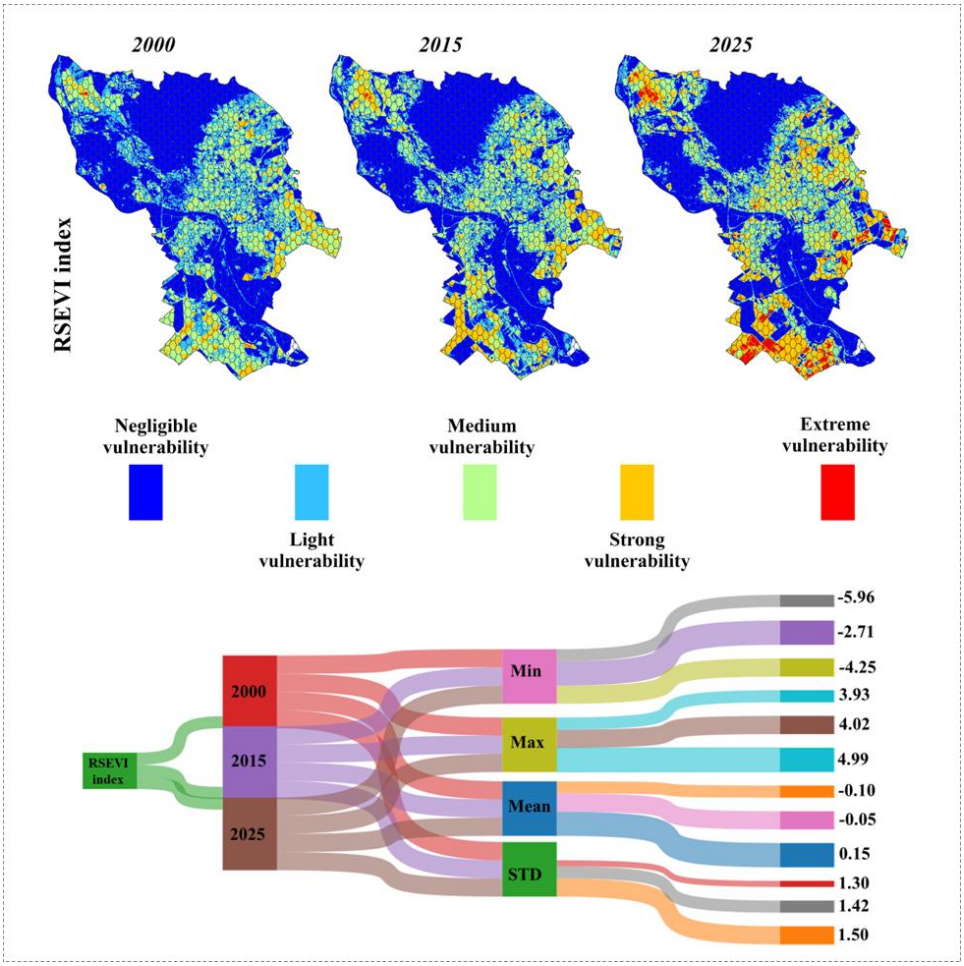

Fig 4. Synthesis of statistical descriptors and spatial heterogeneity of RSEVI-derived vulnerability classes over time (2000–2025), illustrating the progression from negligible to extreme vulnerability.

however, a noticeable expansion of medium (light green) and strong (yellow) vulnerability was observed, particularly across the peripheral and southern parts of the region. This trajectory becomes far more pronounced by 2025, when large portions of the area transition into strong and extreme (red) vulnerability categories. The eastern and southern subregions emerged as critical hotspots, reflecting both intensified environmental stressors and insufficient adaptive capacity. The progression from negligible vulnerability in 2000 to widespread extreme conditions in 2025 illustrates systemic destabilization, whereby the region is increasingly exposed to environmental risks and socio-ecological fragility. Such spatiotemporal dynamics highlight the structural deepening of vulnerability and the urgent need for targeted management strategies and resilience-building policies. Without proactive intervention, the observed trajectory strongly suggests that the study area may face compounded risks, where ecological pressures and social sensitivities converge to amplify systemic instability.

Spatiotemporal Patterns of the DI and the Evolution of Thermal Stress across Three Time Periods

The spatiotemporal evolution of the DI between 2000 and 2025 reveals a clear and statistically meaningful intensification of thermal stress across the study area. In 2000, the DI values ranged from 13.01 to 38.71, with a mean of 23.31. Both the numerical evidence and corresponding spatial representation indicate that most of the area remained within no discomfort or mild discomfort zones, with only a few localized hotspots approaching critical thresholds. By 2015, although the maximum DI increased only marginally to 38.99 and the mean rose slightly to 24.29, the maps distinctly illustrate the spatial expansion of zones where general discomfort became dominant. This shift suggests that the progression of thermal stress is not only numerical, but also strongly geographical, reflecting an increasing proportion of the population exposed to adverse conditions. The situation escalates dramatically by 2025, when the DI reaches a maximum of 43.38 and the mean climbs to 26.79, accompanied by a rise in standard deviation from 3.21 in 2000 to 3.79. This increase in variance indicates growing spatial heterogeneity and sharp contrasts between relatively safer and severely stressed zones. The corresponding map underscores this transformation, with large contiguous areas transitioning into states of severe thermal stress and medical emergencies. Collectively, the convergence of statistical indicators and spatial patterns underscores the accelerating impact of climate change on thermal comfort, highlighting critical public health risks and the urgent need for adaptive planning, infrastructural interventions, and evidence-based policy responses.

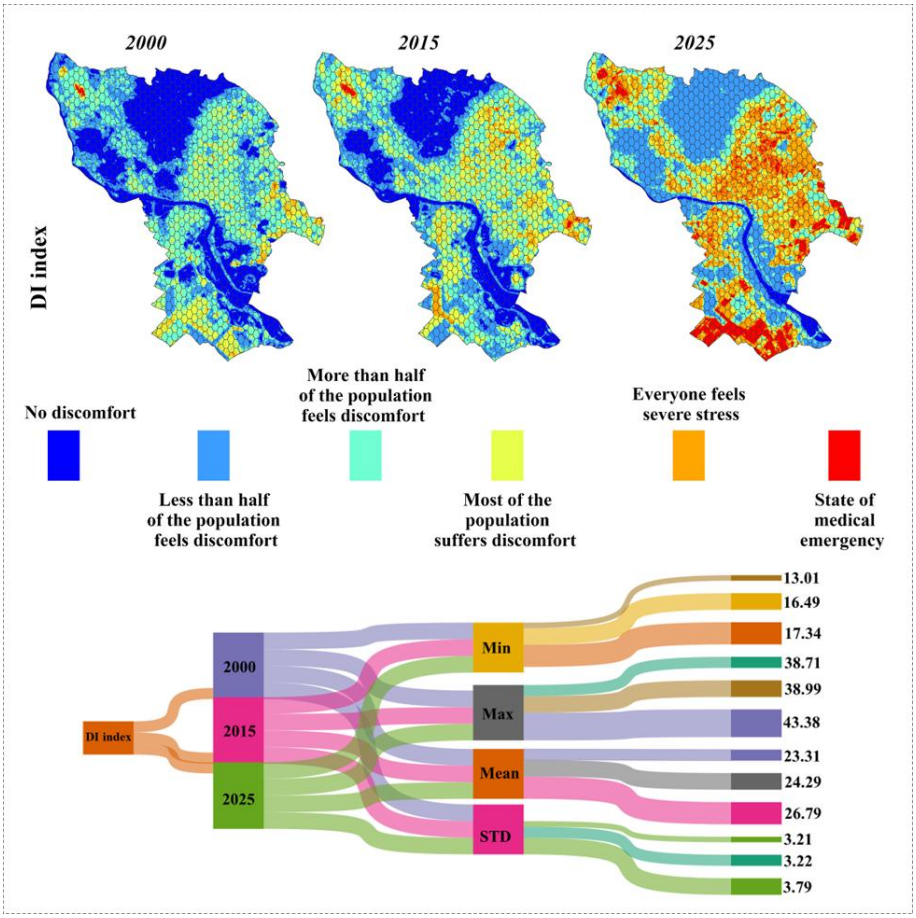

Fig 5. Statistical profiling and temporal variation of DI-based thermal discomfort classes (2000–2025) highlighted the transition from no discomfort to medical emergency conditions.

Spatiotemporal variation in the RSEVI and DI vulnerability classes across 2000, 2015, and 2025.

The temporal dynamics of DI and RSEVI between 2000 and 2025 revealed a clear transition toward higher levels of vulnerability and discomfort across the study area. According to the RSEVI, the proportion of land under negligible vulnerability gradually declined from 48.59% in 2000 to 47.20% in 2025. In contrast, the proportion of areas experiencing strong and extreme vulnerability increased markedly. Specifically, the extent of strong vulnerability rose from 19.98 km² (5.45%) in 2000 to 59.54 km² (16.23%) in 2025, while extreme vulnerability expanded from only 0.18 km² (0.05%) to 9.83 km² (2.68%) over the same period. These shifts underscore the progressive drift of the landscape toward more fragile and risk-prone conditions. Similarly, the DI index demonstrated a parallel trajectory of intensifying stress. Areas categorized as experiencing no discomfort declined sharply, from 29.70% in 2000 to 2.91% in 2025. Conversely, everyone felt severe stress, and the state of medical emergency exhibited substantial increases, rising from 1.86% and 0.10% in 2000 to 25.60% and 8.62% in 2025, respectively. Such transformations strongly indicate a significant deterioration in thermal comfort and human well-being, reflecting escalating environmental pressures within the region. Overall, the concurrent trends in DI and RSEVI highlight a pronounced shift from relatively stable and resilient conditions in 2000 to a highly vulnerable and discomfort-prone state by 2025. This trajectory not only underscores the urgent need for climate-responsive adaptation strategies but also emphasizes the importance of integrated environmental management and policy interventions to mitigate the adverse consequences of these transitions (Table 4).

Table 4. Spatiotemporal variation in the areal extent (km²) of the RSEVI and DI vulnerability classes across 2000, 2015, and 2025.

RSEVI index Area (km^2)			
Year	2000	2015	2025
Categories	Area (km^2)		
Negligible vulnerability	178.22	176.21	173.12
Light vulnerability	80.69	67.08	52.4
Medium vulnerability	87.68	84.69	71.86
Strong vulnerability	19.98	38.46	59.54
Extreme vulnerability	0.18	0.31	9.83
DI index Area (km^2)			
No discomfort	108.94	84.29	10.66
Less than half of the population feels discomfort	90.02	84.55	106.01
More than half of the population feels discomfort	119.81	107.26	68.77
Most of the population suffers discomfort	40.78	71.98	55.79
Everyone feels severe stress	6.82	17.61	93.89
State of medical emergency	0.38	1.06	31.63

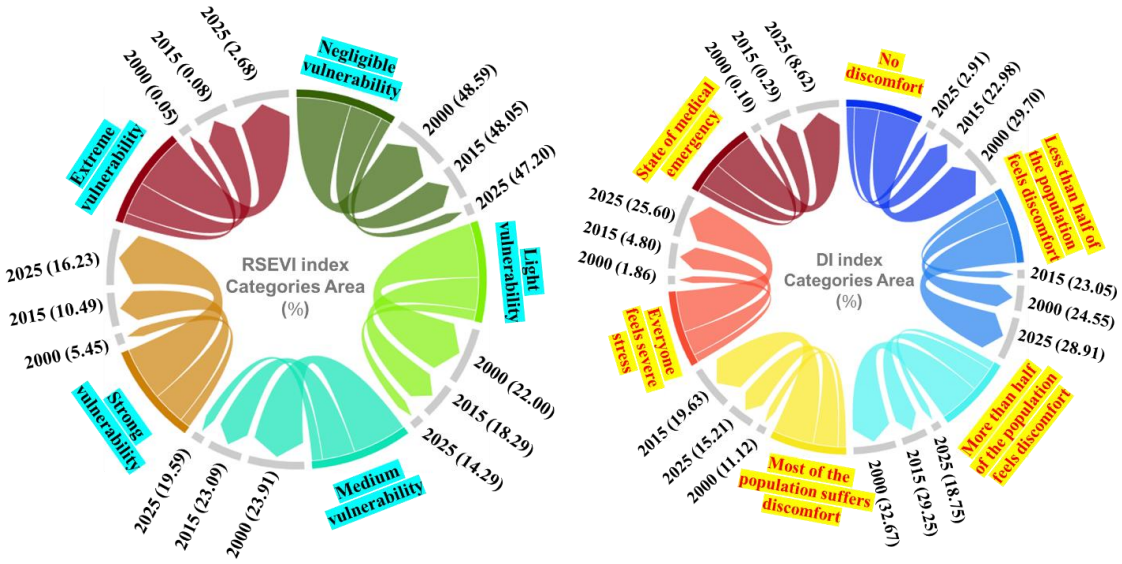

Fig 6. Percentage distribution of RSEVI and DI vulnerability classes, highlighting temporal shifts in relative proportions during 2000, 2015, and 2025.

Spatial Clustering Dynamics between the DI and RSEVI: Evidence of Dual Trajectories of Vulnerability and Resilience

The spatial maps and statistical outputs derived from the bivariate local association (Lee's L) DI and RSEVI reveal a relationship that, while statistically robust, is profoundly heterogeneous and clustered. In the southern, southeastern, and southwestern regions, as well as parts of the northern sector, high-high clusters occupy a

substantial portion of the spatial domain, with their prevalence increasing markedly from 0.48 in 2000 to 0.74 in 2025. This sharp rise indicates the intensification of zones where elevated discomfort levels coincide with poor ecological performance, transforming these areas into critical hotspots of climatic stress and environmental degradation. In contrast, the northern, northwestern, and parts of the southern areas are predominantly characterized by low-low clusters, which increase from 0.23 in 2000 to 0.34 in 2025. These clusters represent zones of relative resilience, where lower climatic discomfort coexists with favorable ecological conditions, and thus can be interpreted as socio-ecological strongholds of stability. In the western and central regions, patches of high-low associations persist with relative temporal stability (approximately 0.39 in both 2015 and 2025). These clusters reflect areas where severe discomfort is experienced despite ecologically favorable conditions, highlighting climatic stressors that operate independently of ecological capacity. Conversely, the share of low-high clusters exhibits a notable increase, rising from 0.28 in 2000 to 0.48 in 2025. These associations delineate areas where ecological fragility and vegetation degradation occur despite low levels of discomfort, thereby signaling zones that are highly vulnerable from an environmental standpoint and necessitating targeted ecological protection policies.

From a statistical perspective, the significance levels further reinforced these interpretations. In 2000, approximately 94% of the associations were significant at the 99% confidence level, which increased to 96% by 2025. Similarly, significant associations at the 95% level rose from 0.85 in 2000 to 0.90 in 2025, reflecting a strengthening of the spatial coupling between DI and RSEVI over time. Nevertheless, the share of non-significant associations also grew, from 0.68 in 2000 to 0.83 in 2025, particularly in the central and boundary regions. These areas can be seen as transitional or structurally shifting zones, where the relationship between discomfort and ecological conditions is weakening or undergoing reconfiguration.

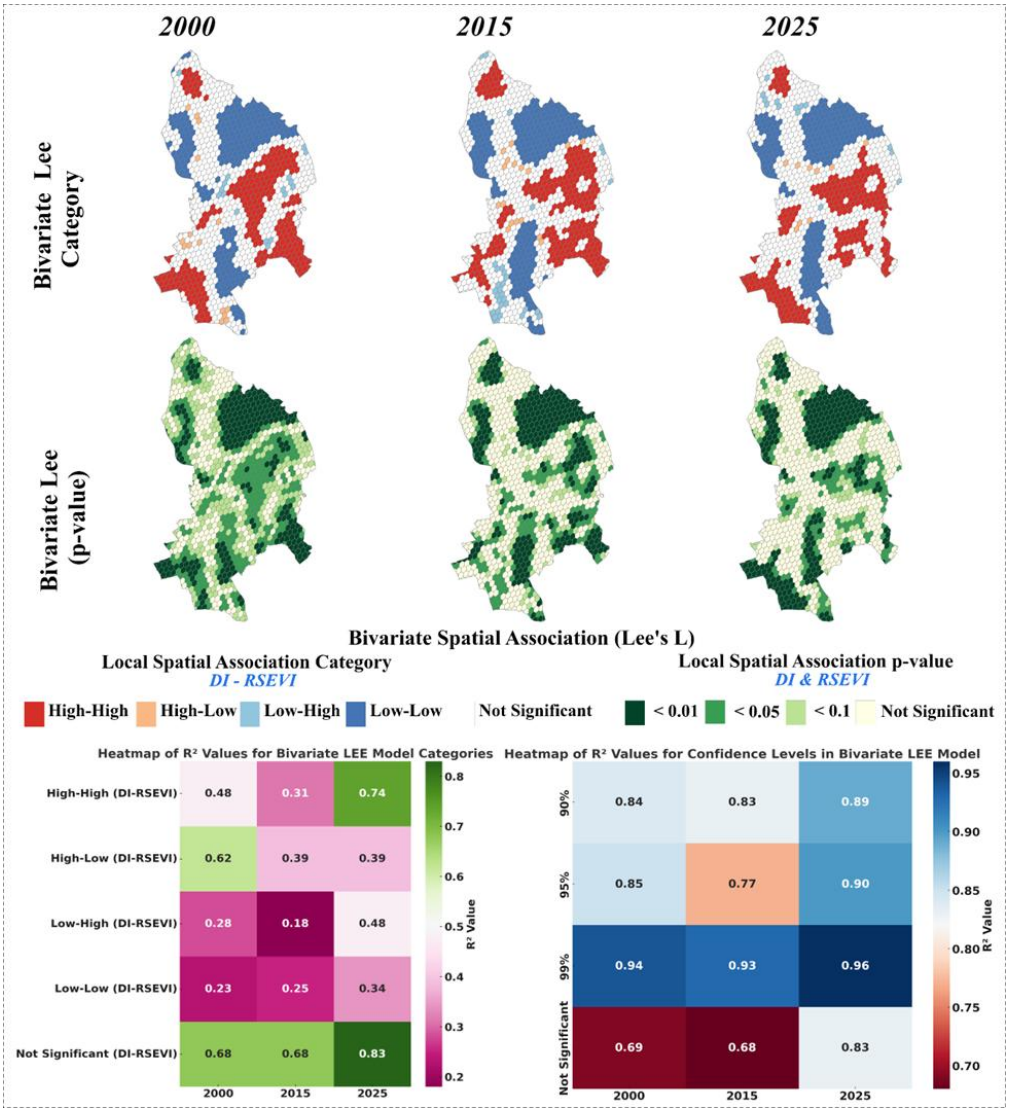

Fig 7. Spatial distribution, temporal variation, and statistical significance of Lee's bivariate local association categories (high–High, Low–Low, High–Low, and Low–high) between the DI and RSEVI across study regions for 2000, 2015, and 2025, highlighting the intensification of high–high hotspots and consolidation of low–low resilient zones over time.

Overall, the findings delineate clear spatial duality. On the one hand, the intensity and extent of critical high-high and low-high clusters are expanding, thereby magnifying the convergence of climatic stress and ecological vulnerability. In contrast, low-low clusters are consolidated as resilient cores, representing domains of ecological and climatic stability. This duality underscores the coexistence of escalating hotspots of socio-ecological risk alongside emerging pockets of resilience, highlighting the urgent need for spatially differentiated and context-sensitive climate–ecological policy interventions.

Spatio-Temporal Dynamics of the Bivariate Relationship between DI and RSEVI (2000–2025)

The figure presents the results of a bivariate spatial relationship analysis between DI and RSEVI across three time periods: 2000, 2015, and 2025. The results clearly revealed substantial temporal shifts in the co-occurrence patterns of the two indices. In 2000, a significant proportion of the areas was classified as low–low, reflecting the simultaneous presence of low development pressure and low ecological vulnerability. However, from 2015 onwards, the spatial distribution progressively shifted toward the High–High category, indicating a growing prevalence of areas where elevated development levels co-occurred with intensified ecological stress. This transition underscores the strengthening of the spatial correlation between development processes and ecological degradation over time.

The accompanying donut charts provide quantitative depictions of the relative proportions of each spatial relationship category. A clear trend emerges: while the proportion of low-low areas has gradually declined, the share of high-high clusters has increased considerably, rising from approximately 27.98% in 2000 to 29.61% in 2025. In contrast, the proportion of discordant categories (high-low and low-high) remained relatively stable, with only minor fluctuations throughout the study period. Overall, these findings emphasize that the study period not only witnessed a spatial convergence between development intensity and ecological vulnerability, but also revealed an amplification of this convergence in critical regions, particularly by 2025. Unbalanced development trajectories are directly associated with heightened ecological degradation, raising significant managerial and policy implications for sustainable development and environmental protection.

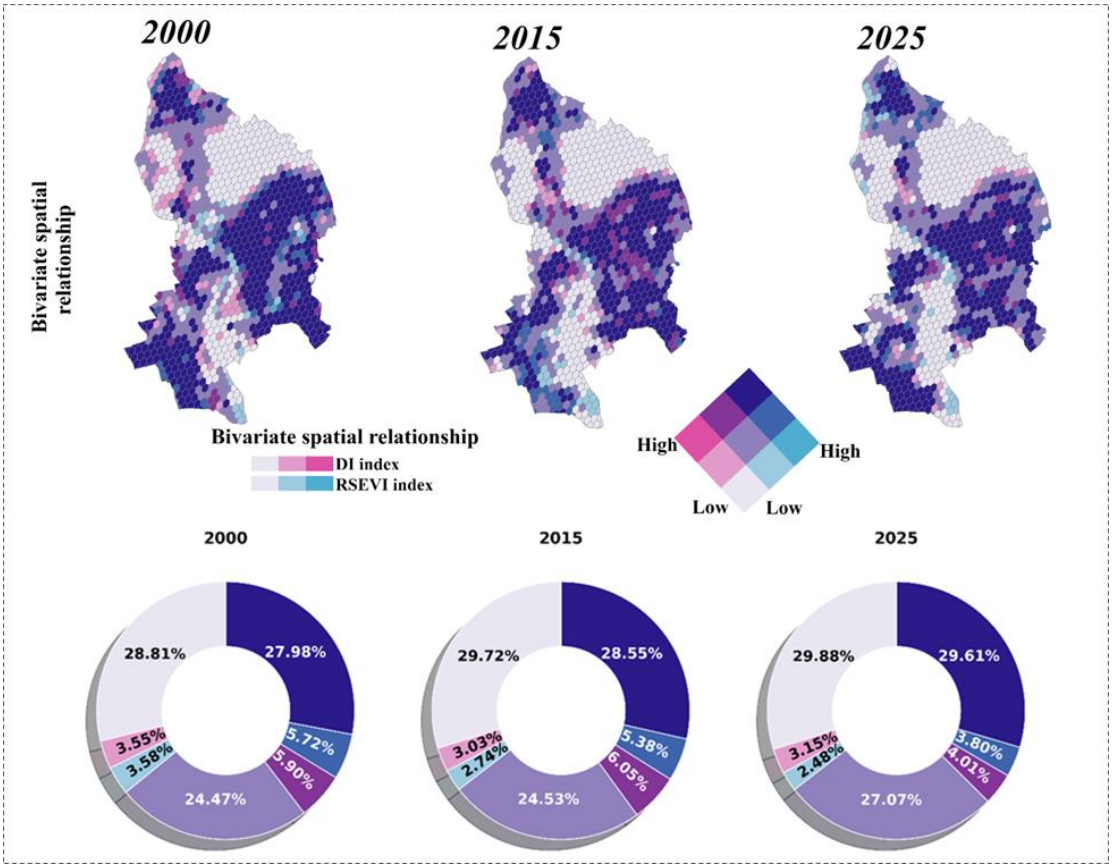

Fig 8. Combined Spatial and Statistical Representation of DI–RSEVI Bivariate Relationships (2000–2025)

Discussion

The spatiotemporal dynamics of the RSEVI between 2000 and 2025 revealed systemic deterioration in the study area. The fluctuations in minimum values (–5.96 2000, –2.71 2015, and –4.26 in 2025), along with steadily increasing maximum values (3.93 to 5.00), an upward drift in mean values (–0.10 to 0.15), and rising standard deviation (1.31 to 1.50), collectively illustrate the dual phenomenon of intensifying ecological fragility and widening heterogeneity. These trends mirror the findings in the Yellow River Basin (Guo et al., 2024; Han et al., 2025), where climate stress combined with human activities exacerbates vulnerability. Similarly, Niu et al. (2024) documented that land use changes and rapid urban expansion resulted in divergent spatial patterns of ecological fragility, reinforcing our observation of increasing spatial disparity. The expansion of built-up areas in our study region has severely degraded vegetation cover, a process highlighted by Wen et al. (2023), further accelerating ecological vulnerability. In contrast, He et al. (2023) reported that targeted ecological restoration and sustainable land-use practices stabilized or even reduced vulnerability in certain Chinese landscapes. This divergence underscores the critical role of proactive ecological governance. The absence of comparable large-scale ecological restoration programs in our study area suggests that anthropogenic pressures outpace adaptive interventions, resulting in unchecked vulnerability growth.

DI showed a parallel escalation trajectory. The mean DI increased from 23.31 in 2000 to 26.79 in 2025, the maximum DI rose from 38.71 to 43.38, and the share of "no discomfort" zones plummeted from 29.70% to just 2.91%, while medical-emergency zones surged from 0.10% to 8.62%. These findings are consistent with observations from the Arabian Peninsula, where intensified heat stress and extreme events have been documented (Ullah et al. 2024). Our results are consistent with those of Imran et al. (2021), who found that urban sprawl and the conversion of vegetated land to built-up and wasteland areas significantly increased human thermal discomfort.

The class transitions in ecological vulnerability provided further evidence for this deterioration. Negligible vulnerability areas decreased modestly (48.59% to 47.20%), strong vulnerability more than tripled (5.45% to 16.23%), and extreme vulnerability surged fifty-fold (0.05% to 2.68%). Comparable results were reported by Dong et al. (2025), who observed expanding fragile zones in northern China even in the presence of conservation efforts. Similarly, Zhang (2021, 2024) noted an increasing prevalence of mild, moderate, and strong vulnerability classes in different regions of China. Again, the inconsistencies with He et al. (2023) highlight the potential for divergence in trajectories depending on the extent and efficacy of ecological governance.

Our findings demonstrate a substantial expansion of high-high clusters (areas characterized by elevated discomfort coupled with high ecological vulnerability), particularly across the southern, southeastern, southwestern, and selected northern regions. The prevalence of these clusters has increased markedly from approximately 0.48 in 2000 to approximately 0.74 in 2025, underscoring the intensification of socio-ecological hotspots. In parallel, Low–Low clusters (low discomfort and low ecological vulnerability) also exhibited a moderate increase, rising from nearly 0.23 to 0.34, which suggests the consolidation of resilience cores within the system. In contrast, high-low clusters remained relatively stable over time (~0.39 in both 2015 and 2025), indicating areas where discomfort intensified despite ecologically favorable conditions. Conversely, low-high clusters expanded considerably, increasing from ~0.28 in 2000 to ~0.48 in 2025, reflecting regions where ecological vulnerability has worsened despite relatively low levels of climatic discomfort. These patterns are partially inconsistent with the results of Zhang et al. (2023), who reported a contraction of both high-high and low-low clusters within their study domain.

Taken together, these findings emphasize the systemic destabilization of both ecological systems and human comfort in the study area. They also highlight the duality of risk and resilience: while vulnerability hotspots are intensifying, small pockets of resilience remain, offering opportunities for targeted interventions.

Policy Implications

The findings of this study have profound implications for environmental policies and adaptive management. The transition from relatively stable ecological and climatic conditions in 2000 toward heightened fragility and intensified thermal stress in 2025 is neither linear nor homogeneous but is characterized by abrupt spatial and temporal shifts. For instance, the drastic reduction in no-discomfort zones from 29.70% in 2000 to only 2.91% in 2025, coupled with the sharp escalation of medical emergency areas from 0.10% to 8.62%, reflects an unfolding crisis with direct consequences for public health and social resilience. Similarly, the expansion of strongly and extremely fragile ecological zones from 5.45% and 0.05% in 2000 to 16.23% and 2.68% in 2025, respectively, signifies an urgent demand for spatially differentiated policies. These results underscore the need to design context-sensitive strategies that simultaneously target high-risk hotspots (high-high clusters) and safeguard resilient zones (low-low clusters). Particularly in the southern and eastern subregions, where vulnerability hotspots are consolidating, proactive interventions in natural resource management, cooling infrastructure, and adaptive capacity building emerge as indispensable priorities.

Contributions

This research advances the scientific literature in two ways. First, by integrating the RSEVI and DI indices through bivariate spatial analysis (Lee's L), heterogeneous clusters of convergence and divergence would have remained invisible in univariate assessments. Second, the provision of robust statistical evidence, such as the upward shift in mean RSEVI from –0.10 in 2000 to 0.15 in 2025 and in mean DI from 23.31 to 26.79, demonstrates a systemic drift toward greater heterogeneity and intensification of risks. Together, these contributions enrich the empirical understanding of socio-ecological vulnerability while providing a novel analytical framework for reassessing resilience theory in climate–ecological systems.

Limitations

Despite its contributions, this study had several limitations. The reliance on composite indices, while methodologically robust, may obscure microscale dynamics and localized drivers of vulnerability. Furthermore, dependence on reanalysis datasets introduces potential biases arising from scale mismatches or sparse local observations. Finally, the focus of the analysis was predominantly biophysical and spatiotemporal, with less attention paid to institutional, economic, and behavioral dimensions that fundamentally shape vulnerability and adaptive capacity. These limitations highlight the need for caution when generalizing the results beyond a specific study area.

Future Research Directions

Future investigations could address these limitations in three main ways. First, the integration of remote sensing indicators with participatory and field-based data collection allows for more holistic and multiscalar narratives of vulnerability. Second, developing scenario-based predictive models that integrate climate projections and socioeconomic trajectories could enhance foresight into possible futures. Third, embedding institutional and governance factors into analytical models, particularly in relation to policy interventions that either mitigate or exacerbate high–High and Low–high clusters, would strengthen the bridge between science and policy. Such efforts would contribute to advancing spatially informed, justice-oriented adaptation strategies.

Conclusions

In conclusion, this study demonstrated a clear and statistically significant transition from relative stability in 2000 to heightened socio-ecological fragility and thermal discomfort by 2025. Numerical evidence underscores the severity of this transformation: no-discomfort zones declined from 29.70% to 2.91%, strongly fragile areas increased from 5.45% to 16.23%, and medical emergency zones expanded dramatically from 0.10% to 8.62%. These shifts indicate not only ecological destabilization but also a direct threat to human well-being. The simultaneous consolidation of high-high clusters and the persistence of low-high associations further reveal the convergence of climatic stress and ecological degradation in critical subregions. Without targeted and evidence-based interventions, widening disparities between resilient and fragile zones is likely to deepen systemic vulnerabilities. By offering both quantitative evidence and spatially nuanced insights, this study highlights the urgent necessity of climate-responsive policies, spatially differentiated management strategies, and integrated resilience-building frameworks while laying the groundwork for future interdisciplinary research at the interface of vulnerability, resilience, and spatial justice.

References

Aghazadeh, F., Mashayekh, H., Akbari, M. A., Boroukanlou, S., Habibzadeh, N., Ghasemi, M., & Goswami, A. (2025). A GIRS-based analysis of urban green space losses with land-use changes and its relationship with surface urban heat island in the city of Tabriz. Advances in Space Research, 75(2), 1804-1824.

Aghazadeh, F., Rahimi, A., Tarashkar, M., Firozjaei, M. K., Ioja, C., Ondrejicka, V., & Finka, M. (2025). Assessing the Green Infrastructure and Built Up effects in Enhancing Thermal Comfort for Vulnerable Populations in Urban Heat Waves: A Case Study of Tabriz Metropolitan. Remote Sensing Applications: Society and Environment, 101671.

Aghazadeh, F., Samadi, M., Cheval, S., & Moshiri, S. (2025). Impacts of land use, vegetation, and air pollution on surface urban heat island spatiotemporal dynamics: Tehran as a case study. International Journal of Environmental Science and Technology, 1-27.

Alonso, L., & Renard, F. (2020). A comparative study of the physiological and socioeconomic vulnerabilities to heat waves of the population of the metropolis of Lyon (France) in a climate change context. International journal of environmental research and public health, 17(3), 1004.

Alyaqout, A., & Anzah, F. (2025). Application of bivariate mapping to assess geodiversity and its geomorphic constraints: A case study in Kuwait. International Journal of Geoheritage and Parks, 13(1), 17-30.

Ameur, M., Habba, M., & Jabrane, Y. (2019). A comparative study of nature inspired optimization algorithms on multilevel thresholding image segmentation. Multimedia Tools and Applications, 78(24), 34353-34372.

Anselin, L. (1995). Local indicators of spatial association—LISA. Geographical analysis, 27(2), 93-115.

Anselin, L. (2019). GeoDa workbook. Global Spatial Autocorrelation. Available online: https://geodacenter. github. io/workbook/5a_global_auto/lab5a. html# morans-i (accessed on: 17/01/2021).

Bahta, Y. T., Jordaan, A., & Muyambo, F. (2016). Communal farmers' perception of drought in South Africa: Policy implication for drought risk reduction. International Journal of Disaster Risk Reduction, 20, 39-50

Bai, X., Zhang, Z., Li, Z., & Zhang, J. (2023). Spatial heterogeneity and formation mechanism of eco-environmental quality in the Yellow River Basin. Sustainability, 15(14), 10878.

Belčáková I, Slámová M, Demovičová Z (2022) Importance of urban green areas in the context of current and future global changes: lessons learned from a case study in Bratislava (Slovakia). Sustainability 14:14740. https://doi.org/10.3390/su142214740.

Bobáľová, H., Falťan, V., Benová, A., Kožuch, M., Kotianová, M., & Petrovič, F. (2024). Measuring the quality and accessibility of urban greenery using free data sources: A case study in Bratislava, Slovakia. Urban Forestry & Urban Greening, 93, 128217.Bonshoms, M., Ubeda, J., Liguori, G., Körner, P., Navarro, Á., & Cruz, R. (2022). Validation of ERA5-Land temperature and relative humidity on four Peruvian glaciers using on-glacier observations. Journal of Mountain Science, 19(7), 1849-1873.

Brewer, C. A. (2016). Designing better maps: A guide for GIS users (Second edition). Esri Press.

Chen, L., Shen, S., Song, C., & Zhao, M. (2025). Estimating the urban ecological quality on the Qinghai–Tibet Plateau using a spatiotemporal remote sensing ecological index. Ecological Frontiers.

Comite'Europe'en de Normalisation, C. E. N. (2007). Indoor environmental input parameters for design and assessment of energy performance of buildings addressing indoor air quality, thermal environment, lighting and acoustics. EN 15251.

Da Silva, V. D. P. R., de Azevedo, P. V., Brito, R. S., & da Cunha Campos, J. H. B. (2010). Evaluating the urban climate of a typically tropical city of northeastern Brazil. Environmental monitoring and assessment, 161(1), 45-59.

Dinerstein, E., Vynne, C., Sala, E., Joshi, A. R., Fernando, S., Lovejoy, T. E., ... & Wikramanayake, E. (2019). A global deal for nature: Guiding principles, milestones, and targets. Science advances, 5(4), eaaw2869. https://doi.org/10.1126/sciadv.aaw2869 (Science)

Dong, M., Zhang, Q., Wang, Q., Jing, C., & Luo, H. (2025). Spatiotemporal distribution and driving forces of ecological fragility in Chengde's transitional region from plateau to plain, China. Environmental Monitoring and Assessment, 197(8), 897.

Ebi, K. L., Kovats, R. S., & Menne, B. (2006). An approach for assessing human health vulnerability and public health interventions to adapt to climate change. Environmental health perspectives, 114(12), 1930-1934.

Ekra, A. T., Hamed, M. M., Ali, Z., Muhammad, M. K. I. B., Khan, M. M. H., Kamruzzaman, M., & Shahid, S. (2024). Changes in human heat discomfort and its drivers in Bangladesh. Urban Climate, 55, 101884.

Gao, Y., & Zhang, H. (2018). The study of ecological environment fragility based on remote sensing and GIS. Journal of the Indian society of remote sensing, 46(5), 793-799.

Guo, B., & Wen, Y. (2019). An optimal monitoring model of desertification in Naiman banner based on feature space utilizing Landsat8 OLI image. IEEE Access, 8, 4761-4768.

Guo, B., Xu, M., Zhang, R., & Luo, W. (2024). A new monitoring index for ecological vulnerability and its application in the Yellow River Basin, China from 2000 to 2022. Journal of Arid Land, 16(9), 1163-1182.

Guo, B., Xu, M., Zhang, R., & Luo, W. (2024). A new monitoring index for ecological vulnerability and its application in the Yellow River Basin, China from 2000 to 2022. Journal of Arid Land, 16(9), 1163-1182.

Guo, B., Zang, W., & Luo, W. (2020). Spatial-temporal shifts of ecological vulnerability of Karst Mountain ecosystem-impacts of global change and anthropogenic interference. Science of the total environment, 741, 140256.

Guo, B., Zang, W., Yang, F., Han, B., Chen, S., Liu, Y., ... & Gong, R. (2020). Spatial and temporal change patterns of net primary productivity and its response to climate change in the Qinghai-Tibet Plateau of China from 2000 to 2015. Journal of Arid Land, 12(1), 1-17. Li, Q., Shi, X., & Wu, Q. (2021). Effects of protection and restoration on reducing ecological vulnerability. Science of the Total Environment, 761, 143180.

Han, J., Guo, B., Pan, L., Han, B., & Xu, T. (2025). Change Patterns of Ecological Vulnerability and Its Dominant Factors in Mongolia During 2000–2022. Remote Sensing, 17(7), 1248.

Han, J., Guo, B., Pan, L., Han, B., & Xu, T. (2025). Change Patterns of Ecological Vulnerability and Its Dominant Factors in Mongolia During 2000–2022. Remote Sensing, 17(7), 1248.

He, D., Hou, K., Li, X. X., Wu, S. Q., & Ma, L. X. (2023). A reliable ecological vulnerability approach based on the construction of optimal evaluation systems and evolutionary tracking models. Journal of Cleaner Production, 419, 138246.

He, G., Bao, K., Wang, W., Zhu, Y., Li, S., & Jin, L. (2021). Assessment of ecological vulnerability of resource-based cities based on entropy-set pair analysis. Environmental technology, 42(12), 1874-1884.

Hu, X., Ma, C., Huang, P., & Guo, X. (2021). Ecological vulnerability assessment based on AHP-PSR method and analysis of its single parameter sensitivity and spatial autocorrelation for ecological protection–A case of Weifang City, China. Ecological Indicators, 125, 107464.

Huang, B., Zha, R., Chen, S., Zha, X., & Jiang, X. (2023). Fuzzy evaluation of ecological vulnerability based on the SRP-SES method and analysis of multiple decision-making attitudes based on OWA operators: A case of Fujian Province, China. Ecological Indicators, 153, 110432.

Huang, J., Zhong, P., Zhang, J., & Zhang, L. (2023). Spatial-temporal differentiation and driving factors of ecological resilience in the Yellow River Basin, China. Ecological Indicators, 154, 110763.

Illanas, S., Gómez-Rubio, V., Vicente, J., & Acevedo, P. (2025). Assessment of bivariate relationships between spatial patterns: Revisiting the global and local L bivariate indices for wildlife management and conservation. Ecological Indicators, 175, 113551.

Imran, H. M., Hossain, A., Islam, A. S., Rahman, A., Bhuiyan, M. A. E., Paul, S., & Alam, A. (2021). Impact of land cover changes on land surface temperature and human thermal comfort in Dhaka city of Bangladesh. Earth Systems and Environment, 5(3), 667-693.

Jankowski, P., Şalap-Ayça, S., Najwer, A., Ligmann-Zielińska, A., & Zwoliński, Z. (2024). Effectiveness of Adjacent and Bivariate Maps in Communicating Global Sensitivity Analysis for Geodiversity Assessment. ISPRS International Journal of Geo-Information, 13(6), 199.

Kang, H., Tao, W., Chang, Y., Zhang, Y., Xuxiang, L., & Chen, P. (2018). A feasible method for the division of ecological vulnerability and its driving forces in Southern Shaanxi. Journal of Cleaner Production, 205, 619-628.

Lee, S. I. (2001). Developing a bivariate spatial association measure: an integration of Pearson's r and Moran's I. Journal of geographical systems, 3(4), 369-385.

Lee, S. I. (2001). Developing a bivariate spatial association measure: an integration of Pearson's r and Moran's I. Journal of geographical systems, 3, 369-385.

Lee, S. I. (2017). Correlation and Spatial Autocorrelation. Encyclopedia of GIS, 1, 360-368.

Lin, Z., Liu, Y., Wen, Z., Chen, X., Han, P., Zheng, C., ... & Shi, H. (2023). Spatial–temporal variation characteristics and driving factors of net primary production in the Yellow River Basin over multiple time scales. Remote Sensing, 15(22), 5273.

Lu, Z., Leigang, S., Quanhong, X. U., Jianfeng, L. I. U., & Xiaoqian, M. A. (2022). MODIS-based comprehensive assessment and spatial-temporal change monitoring of ecological quality in Beijing-Tianjin-Hebei region. Remote Sensing for Natural Resources, 34(2).

Lucas, K., Dewitt, B., Biddle, D. J., & Zhang, C. H. (2025). A Spatial Analysis of the Association Between Urban Heat and Coronary Heart Disease. ISPRS International Journal of Geo-Information, 14(9), 344.

Ma, J., Zhang, C., Guo, H., Chen, W., Yun, W., Gao, L., & Wang, H. (2020). Analyzing ecological vulnerability and vegetation phenology response using NDVI time series data and the BFAST algorithm. Remote Sensing, 12(20), 3371.

Ma, X., de Jong, M., Sun, B., & Bao, X. (2020). Nouveauté or Cliché? Assessment on island ecological vulnerability to tourism: application to Zhoushan, China. Ecological Indicators, 113, 106247.

Monforte, P., & Ragusa, M. A. (2022). Evaluation of bioclimatic discomfort trend in a central area of the mediterranean sea. Climate, 10(10), 146.

Niu, H., Xiu, Z., & Xiao, D. (2024). Impact of land-use change on ecological vulnerability in the Yellow River Basin based on a complex network model. Ecological Indicators, 166, 112212.

Pak, S. S., Ratoza, M., & Cheuy, V. (2024). Examining rehabilitation access disparities: an integrated analysis of electronic health record data and population characteristics through bivariate choropleth mapping. BMC Health Services Research, 24(1), 170.

Patle, S., & Ghuge, V. V. (2024). Urban fragmentation approach for assessing thermal environment dynamics: A case study of semi-arid city from a comfort perspective. Urban Climate, 53, 101784.

Pimm, S. L., Jenkins, C. N., Abell, R., Brooks, T. M., Gittleman, J. L., Joppa, L. N., ... & Sexton, J. O. (2014). The biodiversity of species and their rates of extinction, distribution, and protection. science, 344(6187), 1246752.https://doi.org/10.1126/science.1246752 (Science)

Rees, G., Hebryn-Baidy, L., & Belenok, V. (2024). Temporal variations in land surface temperature within an urban ecosystem: A comprehensive assessment of land use and land cover change in Kharkiv, Ukraine. Remote Sensing, 16(9), 1637.

Santini, L., Butchart, S. H., Rondinini, C., Benítez-López, A., Hilbers, J. P., Schipper, A. M., ... & Huijbregts, M. A. (2019). Applying habitat and population-density models to land-cover time series to inform IUCN Red List assessments. Conservation Biology, 33(5), 1084-1093.

Schlögl, M., Graser, A., Spiekermann, R., Lampert, J., & Steger, S. (2025). Brief communication: Visualizing uncertainties in landslide susceptibility modelling using bivariate mapping. Natural Hazards and Earth System Sciences, 25(4), 1425-1437.

Standard, A.S.H.R.A.E. (1992). Thermal environmental conditions for human occupancy. ANSI/ASHRAE, 55, 5.

Šalkovič, M., & Pauditšová, E. (2023). Use of Satellite Images to determine the temperature of urban surfaces for landscape management purposes, case study Bratislava (Slovak Republic). Land, 12(2), 384.

Tang, Q., Wang, J., & Jing, Z. (2021). Tempo-spatial changes of ecological vulnerability in resource-based urban based on genetic projection pursuit model. Ecological Indicators, 121, 107059.

Tao, R., & Thill, J. C. (2025). A Reciprocal Statistic for Detecting the Full Range of Local Patterns of Bivariate Spatial Association. Annals of the American Association of Geographers, 115(5), 1185-1206.

Thom, E. C. (1959). The discomfort index. Weatherwise, 12(2), 57-61.

Thom, E. C. (1959). The discomfort index. Weatherwise, 12(2), 57-61.

Tian, J., Guo, C., & Wang, J. (2021). Quantitative Assessment of the Ecological Vulnerabiliyt of Baiyangdian Wetlands in the north China Plain [J]. J. Resour. Ecol, 12(06), 814-821.

Ullah, S., Aldossary, A., Ullah, W., & Al-Ghamdi, S. G. (2024). Augmented human thermal discomfort in urban centers of the Arabian Peninsula. Scientific Reports, 14(1), 3974.

Wang Ying, W. Y., Xia WenTao, X. W., Liang TianGang, L. T., & Wang Chao, W. C. (2010). Spatial and temporal dynamic changes of net primary product based on MODIS vegetation index in Gannan grassland.

Wang, P., Zhao, W., & Ke, X. (2021). Evaluation and spatiotemporal evolution of ecological vulnerability of Qianjiang based on SRP model. Research of Soil and Water Conservation, 28(5), 347-354.

Wang, X., Zhang, S., Zhao, X., Shi, S., & Xu, L. (2023). Exploring the relationship between the eco-environmental quality and urbanization by utilizing sentinel and landsat data: A case study of the yellow river basin. Remote Sensing, 15(3), 743.

Wang, Y., Li, X., Zhang, F., Wang, W., & Xiao, R. (2020). Effects of rapid urbanization on ecological functional vulnerability of the land system in Wuhan, China: A flow and stock perspective. Journal of Cleaner Production, 248, 119284.

Wen, B., Huang, C., Zhou, C., Zhang, H., Yang, Q., & Li, M. (2023). Spatiotemporal dynamics and driving factors of soil erosion in the Beiluo River Basin, Loess Plateau, China. Ecological Indicators, 155, 110976.

Worsa-Kozak, M., Górniak-Zimroz, J., Szrek, A., & Chudy, K. (2024). Remote detection and monitoring of post-mining heat island. Frontiers in Environmental Science, 12, 1305149.

Xia, M., Jia, K., Zhao, W., Liu, S., Wei, X., & Wang, B. (2021). Spatio-temporal changes of ecological vulnerability across the Qinghai-Tibetan Plateau. Ecological Indicators, 123, 107274.

Xu, E., Zhang, G., Wang, H., Yang, M., Tian, H., Zhao, M., ... & Wei, D. (2025). Monitoring and Assessing Ecological Environmental Quality in Qianping Reservoir, Central China: A Remote Sensing Ecological Index (RSEI) Approach. Forests, 16(5), 831.

Xu, H., Hu, X., Guan, H., & He, G. (2017). Development of a fine-scale discomfort index map and its application in measuring living environments using remotely-sensed thermal infrared imagery. Energy and Buildings, 150, 598-607.

Yang, Y., & Song, G. (2021). Human disturbance changes based on spatiotemporal heterogeneity of regional ecological vulnerability: A case study of Qiqihaer city, northwestern Songnen Plain, China. Journal of Cleaner Production, 291, 125262.

You, G., Chen, T., Shen, P., & Hu, Y. (2023). Designing an ecological network in Yichang Central City in China based on habitat quality assessment. Sustainability, 15(10), 8313.

Yuan, D., Du, M., Yan, C., Wang, J., Wang, C., Zhu, Y., ... & Kou, Y. (2024). Coupling coordination degree analysis and spatiotemporal heterogeneity between water ecosystem service value and water system in Yellow River Basin cities. Ecological Informatics, 79, 102440.

Zeng, P., Liu, Y., Tian, T., Che, Y., & Helbich, M. (2024). Geographic inequalities in park visits to mitigate thermal discomfort: A novel approach based on thermal differences and cellular population data. Urban Forestry & Urban Greening, 98, 128419.

Zhang, F., Liu, X., Zhang, J., Wu, R., Ma, Q., & Chen, Y. (2017). Ecological vulnerability assessment based on multi-sources data and SD model in Yinma River Basin, China. Ecological Modelling, 349, 41-50.

Zhang, J. C., Gao, P., Dong, X. D., Li, T., Xu, J. W., & Dun, X. J. (2021). Ecological vulnerability assessment of Qingdao coastal zone based on landscape pattern analysis.

Zhang, M., & Qi, S. (2023). The spatio-temporal evolution and driving factors of high-quality development in the Yellow River Basin during the period of 2010–2022. Sustainability, 15(18), 13512.

Zhang, S., Lei, J., Tong, Y., Zhang, X., Lu, D., Fan, L., & Duan, Z. (2023). Temporal and spatial responses of ecological resilience to climate change and human activities in the economic belt on the northern slope of the Tianshan Mountains, China. Journal of Arid Land, 15(10), 1245-1268.

Statistical Office of the Slovak Republic, 2022. The 2021 Population and Housing Census - Selected Data URL 〈https://www.scitanie.sk/storage/app/media/dokumenty/SK582000en.pdf〉